frontiers in Materials

ORIGINAL RESEARCH
published: 25 September 2020
doi: 10.3389/fmats.2020.569723

A Comparative Study on the Thermoelectric Properties of Bismuth Chalcogenide Alloys Synthesized through Mechanochemical Alloying and Microwave-Assisted Solution Synthesis Routes

*Bejan Hamawandi[1], Hamta Mansouri[2], Sedat Ballikaya[3], Yunus Demirci[4], Martina Orlovská[5], Nafiseh Bolghanabadi[2], Seyed Abdolkarim Sajjadi[2] and Muhammet S. Toprak[1]**

[1] Department of Applied Physics, KTH Royal Institute of Technology, Stockholm, Sweden, [2] Department of Materials Science and Engineering, Ferdowsi University of Mashhad, Mashhad, Iran, [3] Department of Physics, Istanbul University, Istanbul, Turkey, [4] Department of Electrical and Electronics Engineering, Istanbul University-Cerrahpasa, Istanbul, Turkey, [5] Department of Inorganic Materials, Slovak University of Technology in Bratislava, Bratislava, Slovakia

OPEN ACCESS

Edited by:
Peter Reiss,
Commissariat à l'Energie Atomique et aux Energies Alternatives (CEA), France

Reviewed by:
Hock Jin Quah,
University of Science Malaysia, Malaysia
Chiyoung Park,
Daegu Gyeongbuk Institute of Science and Technology (DGIST), South Korea
Zhi-Gang Chen,
University of Southern Queensland, Australia

***Correspondence:**
Muhammet S. Toprak
toprak@kth.se

Specialty section:
This article was submitted to Energy Materials, a section of the journal Frontiers in Materials

Received: 04 June 2020
Accepted: 31 August 2020
Published: 25 September 2020

Citation:
Hamawandi B, Mansouri H, Ballikaya S, Demirci Y, Orlovská M, Bolghanabadi N, Sajjadi SA and Toprak MS (2020) A Comparative Study on the Thermoelectric Properties of Bismuth Chalcogenide Alloys Synthesized through Mechanochemical Alloying and Microwave-Assisted Solution Synthesis Routes. Front. Mater. 7:569723. doi: 10.3389/fmats.2020.569723

The way a material is synthesized and processed has an immense effect on its microstructure, which in turn has a big impact on its transport properties. Here, we compare the thermoelectric (TE) properties of n- and p-type $Bi_{2-x}Sb_xTe_3$ (x: 0 and 1.5) materials synthesized through two different routes, specifically mechanochemical alloying (MA)—as a solid-state synthesis route—and microwave(MW)-assisted polyol synthesis—as a solution synthesis route. Reaction time is significantly reduced in the MW synthesis, leading to significantly lower energy consumption (i.e., higher energy efficiency) per batch than using the MA route. The resultant materials are compared for their crystallinity, phase purity, morphology, and microstructure. Spark plasma sintering was used to prepare pellets, and the resultant consolidates were evaluated for their transport properties. TE properties and microstructure of the specimens were investigated in relation to processing conditions and composition. MA samples formed fused structures (from 200 nm to several micrometers in size) composed of smaller particles. MW-synthesized materials exhibited hexagonal platelet morphology, high crystallinity, and phase purity. They also showed lower thermal conductivity, leading to a higher resultant TE figure-of-merit *ZT*. TE properties of $Bi_{2-x}Sb_xTe_3$ samples were studied on sintered cylindrical pellet samples, where the highest *ZT* values achieved were 1.04 (at 440 K) for MW-Bi_2Te_3 and 0.76 (at 523 K) for MW-$Bi_{0.5}Sb_{1.5}Te_3$ samples, while MA-Bi_2Te_3 and MA-$Bi_{0.5}Sb_{1.5}Te_3$ samples showed maximum *ZT* values of 0.74 (at 460 K) and 0.27 (at 300 K), respectively, as n- and p-type TE materials. The observed trend is much higher *ZT* values for MW samples, ascribed to their higher degree of texturing and nanostructured grains reducing the thermal conductivity, thus achieving a better overall performance, verifying the prospect to enhance *ZT* using MW-assisted solution synthesis approach.

Keywords: thermoelectric material, mechanochemical alloying, microwave-assisted reaction, nanostructured thermoelectrics, Seebeck coefficient, electrical conductivity, thermoelectric figure-of-merit ZT

INTRODUCTION

Thermoelectric (TE) materials are capable of directly interconverting heat energy and electrical power. The dimensionless TE figure of merit is a measure of goodness of the materials for TE conversion, which is defined by the following relationship: $ZT = (S^2\sigma T)/\kappa$, where S is the Seebeck coefficient (voltage generated within the material under a temperature gradient), σ is the electrical conductivity, T is the absolute temperature (in K), and κ is the total thermal conductivity [κ_{tot}, defined as the sum of electronic (κ_{el}) and lattice components (κ_{lat})] (Rowe, 2018; Snyder et al., 2010). An ideal TE material is anticipated to have a high power factor ($S^2\sigma$) accompanied with a lower thermal conductivity (κ_{tot}). Based on the temperature range of operation, TE materials can be divided into three classes as ambient, mid-, and high-T materials, where the materials' bandgap and stability determine the viability of a particular composition as a TE material (Snyder et al., 2010). Bismuth telluride (Bi_2Te_3) and its alloys ($Bi_{2-x}Sb_{x2}Se_yTe_{3-y}$) are presently the most promising bulk TE materials, in the ambient temperature region, due to their high TE figure of merit, ZT (Boyer and Cissé, 1992). Low-dimensional materials have been suggested to possess higher TE performance than their bulk counterparts through theoretical analysis and experimental explorations (Dresselhaus et al., 1999; Hicks and Dresselhaus, 1993a; Hicks and Dresselhaus, 1993b). Two physical phenomena underlie the benefit of using nano-sized objects. The first one is the particularities of the electronic structure, which may cause a decrease in the electrical conductivity but at the same time lead to a substantial increase in thermopower; as a result, the power factor ($S^2\sigma$) of nano-sized TEs can be higher than that of their bulk counterparts. Nanostructuring leads to widening of the bandgap with the simultaneous increase in the density of states near the Fermi level. The second phenomenon is the presence of a large number of interfaces (grain boundaries), which may effectively scatter phonons (κ_{lat}) while exerting a minimal effect on the transport of charge carriers (σ), mainly due to the very small size of constituent nano-sized building blocks (Shevelkov, 2008).

Nanomaterials can be synthesized using a diverse set of methodologies, with each method having its limitations and strengths, resulting in materials with the same composition and yet significantly different microstructure. Solid-state transport is shown to be influenced by the microstructure of the resultant materials (Hu et al., 2015; Hu et al., 2018; Bao et al., 2020). A review on the synthesis of nanostructured Bi_2Te_3 has been reported elsewhere, detailing various synthetic methodologies and resultant particle morphologies (Mamur et al., 2018). Bi_2Te_3 is commonly synthesized by using powder metallurgy route, through fusion of elemental bismuth (Bi) and tellurium (Te) metals forming an ingot (Madavali et al., 2016), or *via* mechanochemical synthesis, also known as mechanochemical alloying (MA) (Jang et al., 2018; Liu and Park, 2002). MA is a useful technique for producing both micro- and nanocomposites (Aktas and Diler, 2018). In this method, there are three repeated steps following each other: deformation, cold welding, and fracture. During the milling process, whenever balls collide with each other, some of the powders are trapped in between them. This collision gives energy to the system so that the particles transform physically; in other words, they deform elastically and plastically. Solid-state reactions, normally requiring high temperatures, will occur at much lower temperatures during MA, without needing any external heat. The high defect density induced by intensive milling favors the diffusion process. Particle microstructure refinement, and consequently the reduction in diffusion distances, can significantly reduce the reaction temperatures. Further mechanical treatment can further reduce particle size, enabling the formation of nano-sized powders (Stojanovic et al., 2005). Because of its applicability to essentially synthesize a diverse set of materials, low-cost instrument, and simplicity, MA has become a popular method to synthesize nanocrystalline materials. High-performance nanocomposites have also been prepared using this method for structural and other types of applications (Zakeri et al., 2012). The main advantage of the MA method often quoted is the possibility for easy scaling up of materials for a variety of applications. However, certain disadvantages usually cited were found to be contamination from milling media and/or atmosphere; difficulty in controlling the local temperature/energy during the milling, which causes nonuniform and nonhomogeneous composition including defects and dislocations; and consolidation of powder products without coarsening the nanocrystalline microstructure (Prasad et al., 2018).

Solution chemical synthetic methods may be advantageous for the synthesis of TE materials on a large scale if time- and energy-effective scalable synthetic methods with high reproducibility can be developed. Bi_2Te_3 nanostructures have been reported using solution chemical routes, including solvothermal (Zhang et al., 2015) or hydrothermal, polyol (Li et al., 2010), chemical alloying (Saleemi et al., 2012), and electrochemical (Prieto et al., 2001; Li et al., 2006) methods. Various morphologies including nanoparticles (Cao et al., 2008; Jiang and Zhu, 2007), nanosheets (Shi et al., 2008; Li et al., 2010), films (Li et al., 2006), nanowires (Yu et al., 2004), hollow nanospheres (Li et al., 2006), and nanorods/nanotubes (Prieto et al., 2001, Zhao et al., 2005; Xiao et al., 2007; Li et al., 2009) have been reported. Microwave (MW)-assisted heating has been demonstrated to be practical for the synthesis of binary and ternary TE nanomaterial compositions directly in the solution phase (Kumar et al., 2020; Hamawandi et al., 2020a; Hamawandi et al., 2020b), without needing further processing. Reactions that have lasted several hours to days have been realized in a fraction of the time using MW-assisted heating. There are scarce reports on the use of MW-assisted methods for the synthesis of Bi_2Te_3 (Harpeness and Gedanken, 2003; Zhou et al., 2006; Jiang and Zhu, 2007; Yao et al., 2009; Zhou and Zhu, 2009; Pradhan et al., 2017), with various particle morphologies including hollow spheres, nanosaws, and nanosheets (Jiang and Zhu, 2007). MW irradiation dramatically reduces the energy needed for the synthesis process. Moreover, time is a major issue in chemistry or materials science, due to time-consuming numerous trial-and-error experiments. Time- and energy-efficient synthetic routes are highly sought for in the field of

chemistry/materials science, where a large number of experiments can be conducted within a restricted period of time with reasonable energy consumption (Nüchter et al., 2004). MW reaction time can be shortened to a fraction of conventional synthetic routes, due to special dielectric heating (Anastas and Lankey, 2002). Among the most significant achievements, our recent work demonstrating a scalable MW-assisted synthesis (2 min reaction time) of a series of $Bi_{2-x}Sb_xTe_3$ compounds with moderate to high *ZT* (Hamawandi et al., 2020b) can be listed.

The correlation between the microstructure and final properties of the TE materials has been a topic of intensive research. It is a known fact that the attributes of the building blocks, as well as the adapted consolidation processes, are the major parameters influencing the final microstructure of the material. It is therefore important to further optimize the materials' properties by various synthesis and processing routes to understand in detail the materials' microstructure–property relationships. Here, we present a comparative work on the synthesis of $Bi_{2-x}Sb_xTe_3$ using MA and MW-assisted synthesis routes; the product's crystallinity, the resultant microstructure, their consolidation, and the resultant electronic/thermal transport properties were investigated. Results show a significantly better performance of nanostructured MW-$Bi_{2-x}Sb_xTe_3$ samples.

MATERIALS AND METHODS

Synthesis and Processing of Thermoelectric Materials by Solution Chemical Method

The following chemicals were used for the synthesis reaction: $BiCl_3$ (Sigma Aldrich, 98%, Stockholm, Sweden), $SbCl_3$ (Sigma Aldrich, 99.95%, Stockholm, Sweden), Te powder (Sigma Aldrich, 99.8%, Stockholm, Sweden), ethylene glycol (EG; Sigma Aldrich, 99%), thioglycolic acid (TGA; Sigma Aldrich, 98%, Stockholm, Sweden), and trioctyl phosphine (TOP; Sigma Aldrich, 90%, Stockholm, Sweden). All chemicals were used as received, without further purification.

The synthesis was performed via MW-assisted thermolysis according to the details and mechanism reported earlier (Hamawandi et al., 2020a). Te precursor solution was prepared as a complex with TOP. Bi (or Sb) precursor solution was prepared by dissolving $BiCl_3$ in EG. The stoichiometry of ternary composition was tuned by replacing the $BiCl_3$ precursor with equivalent moles of $SbCl_3$. The two precursor solutions of Te–TOP complex and Bi/Sb-EG were mixed, with the addition of an aliquot of TGA, and transferred to a 100-ml Teflon vessel. The reaction was performed in the MW reactor for 2 min dwell time at 220°C under constant stirring, with a total MW exposure time of 6 min. The product was then cooled down to room temperature. The as-prepared $Bi_{2-x}Sb_xTe_3$ phases were phase-separated from the solvent (EG). Particles were then washed with isopropanol and acetone few times to clean residual chemicals. These samples are designated as MW-$Bi_{2-x}Sb_xTe_3$, where the abbreviation MW stands for "MW-assisted solution synthesis."

TABLE 1 | SPS parameters and transport properties for MW- and MA-$Bi_{2-x}Sb_xTe_3$ samples: sintering temperature (T_{sint}), holding time (t_{hold}), sintering pressure (P_{sint}), bulk density (d_{bulk}), density of pellets by the Archimedes method (d_{pellet}), and packing density (ρ) in percentage of theoretical density.

Sample	T_{sint} (°C)	t_{hold} (min)	P_{sint} (MPa)	d_{bulk} (g/cm^3)	d_{pellet} (g/cm^3)	ρ%
MW-Bi_2Te_3	400	1	50	7.86	6.13	78
MA-Bi_2Te_3	400	10	60	7.86	6.46	82
MW-$Bi_{0.5}Sb_{1.5}Te_3$	400	1	50	6.878	5.36	78
MA-$Bi_{0.5}Sb_{1.5}Te_3$	400	10	60	6.878	5.93	86

Synthesis and Processing of Thermoelectric Materials by Mechanochemical Alloying

The $Bi_{2-x}Sb_xTe_3$ powders were prepared starting from elemental Bi (Sigma Aldrich, 99% purity, Germany), Sb (Sigma Aldrich, 99% purity, Germany), and Te (Sigma Aldrich, 99.8% purity, Germany) powders. These metallic powders exhibited a particle size distribution in the range −150 μm (less than 150 μm) for Bi, −150 μm for Te, and −150 μm for Sb. To make a batch required for stoichiometric $Bi_{2-x}Sb_xTe_3$ composition, corresponding amounts of Bi, Te, and Sb were weighed and loaded into steel jars together with stainless steel milling balls measuring ~8–13 mm in diameter. Synthesis through MA was performed in argon atmosphere in a planetary ball mill (PM 2400, Iran) that was operated at rotation speed of discs with jars ~300 rpm for the Bi_2Te_3 specimen for 4 h and for the $Bi_{0.5}Sb_{1.5}Te_3$ specimen for 12 h. The ball-to-powder weight ratio during milling was 15:1. The samples are designated as MA-$Bi_{2-x}Sb_xTe_3$, where MA stands for "mechanochemically alloyed."

Consolidation via Spark Plasma Sintering

MA- and MW-synthesized TE materials were consolidated using spark plasma sintering (SPS). The SPS parameters, including heating rates, sintering temperature, pressure, and holding time, along with the characteristics of the resultant pellets are presented in detail in **Table 1**. The temperature was set to 400°C, with a heating rate of 30°C/min. Pressure of 60 MPa was used for SPS to densify the final pellets (using a die with an inner diameter of 12 mm). Finally, the pellet was cooled from 400°C to room temperature, while the load was decreased from 60 to 0 MPa. The resultant pellets were then removed from the die for further processing and analysis. **Table 1** summarizes the SPS parameters and the resultant density of obtained pellets.

Structural, Morphological, and Microstructure Characterization

X-ray powder diffraction (XRPD) was used to study the crystallinity, the crystalline phases present, and changes in the structure as a function of processing (SPS sintering) using the PANalytical X'Pert PRO Alpha-1 system, equipped with a copper anode (Cu-$K\alpha_1$ radiation). A step size of 0.24° and a scan speed of 0.04°/s were used in the continuous scan mode. The crystalline phases were identified by using Rietveld

TABLE 2 | Transport properties for MW- and MA-$Bi_{2-x}Sb_xTe_3$ samples: total thermal conductivity (κ_{tot}), Seebeck coefficient (*S*), electrical conductivity (σ), power factor (*PF*), and TE figure of merit (*ZT*) at given temperature (*T*) values. The rightmost column specifies the carrier type.

Sample	*T* (K)	κ_{tot} (W/m K)	*S* (μV/K)	σ (S/m)	*PF* (μWK^2/cm)	*ZT*	Carrier type
MW-Bi_2Te_3	300	0.948	−125	106,356	20.35	0.52	N
	440	0.876	−160	80,018	16.52	1.04	
MA-Bi_2Te_3	300	1.527	−120	122,000	1.76	0.34	N
	460	1.032	−148	75,000	1.65	0.74	
MW-$Bi_{0.5}Sb_{1.5}Te_3$	300	0.856	105	40,077	6.81	0.15	p
	523	0.466	157	27,504	4.41	0.76	
MA-$Bi_{0.5}Sb_{1.5}Te_3$	300	1.742	302	16,700	15.7	0.27	p
	502	1.247	160	18,400	4.72	0.19	

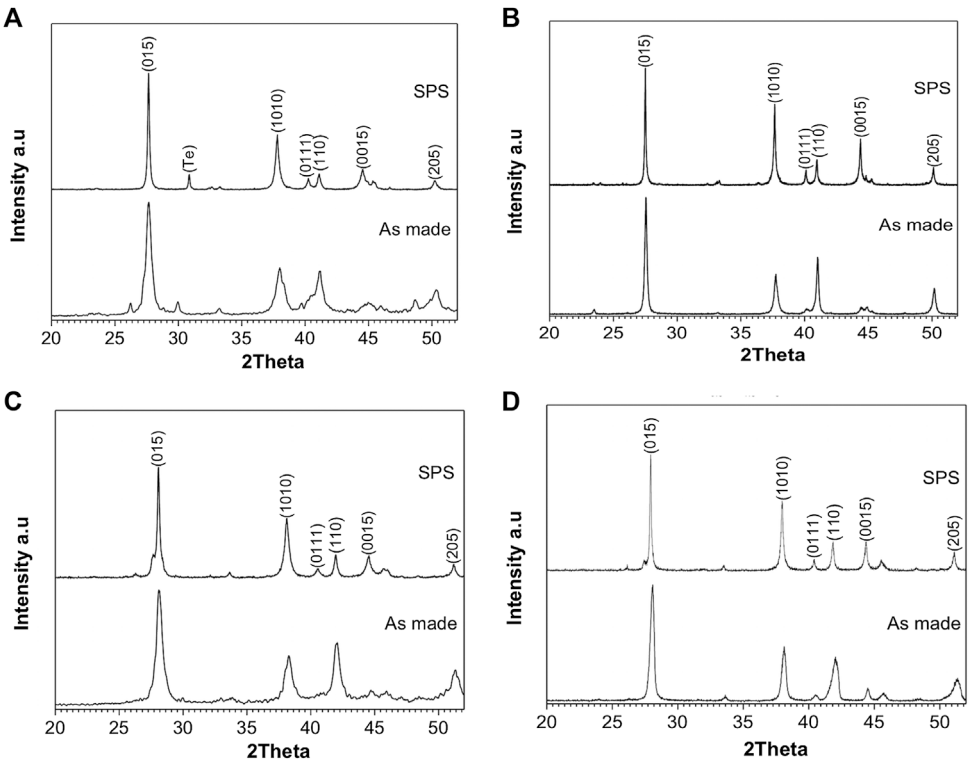

FIGURE 1 | X-ray powder diffraction patterns of as-synthesized and spark plasma sintering (SPS) sintered samples for **(A)** mechanochemical alloying (MA)-Bi_2Te_3, **(B)** microwave-assisted (MW)-Bi_2Te_3, **(C)** MA-$Bi_{0.5}Sb_{1.5}Te_3$, and **(D)** MW-$Bi_{0.5}Sb_{1.5}Te_3$. The crystalline phases are indexed to Bi_2Te_3 (ICDD: 00-015-0863) and $Bi_{0.5}Sb_{1.5}Te_3$ (ICDD: 00-049-1713) with rhombohedral crystal structure.

refinement through MATCH! software. Scanning electron microscopy (SEM; FEI Nova 200 and FE-SEM, TESCAN-BRNO-Mira3 LMU) was used for the investigation of microstructure and morphology of the materials at different process steps.

Transport Property Evaluation

The simultaneous measurements of Seebeck coefficient (*S*) and the electrical conductivity (σ) were performed using an ULVAC-RIKO ZEM3 system (typical error ±%4) on the pellets obtained after the SPS process. The total thermal conductivity κ_{tot} (typical error ±%6) was calculated using the specific heat capacity C_p, thermal diffusivity (α), and density (ρ), through the equation $\kappa_{tot} = C_p \cdot \alpha \cdot \rho$. The density of the samples could be obtained from the Archimedes method; a laser flash analysis system (LFA 1000, Linseis) was used to measure α of disk-shaped samples with nominal dimensions of 2 mm thickness and 12.6 mm diameter. Differential scanning calorimetry (DSC, PT1000, Linseis) was used to measure the specific heat capacity C_p. The thermal range used during the tests ranged from 298 to 523 K, and with all the properties known, the TE figure of merit, *ZT* (typical error ±%8), was estimated. Transport properties of evaluated samples at selected temperatures are summarized in **Table 2**.

RESULTS AND DISCUSSION

Structural Analysis

Structural analysis of synthesized materials was performed using XRPD, and the diffraction patterns for as-made and SPS sintered materials prepared by MA and MW routes are presented in **Figure 1**. As for the sintered samples, XRPD was performed on the pellets' surface perpendicular to the sintering direction. The crystalline phases are indexed to Bi_2Te_3 (ICDD: 00-015-0863) and $Bi_{0.5}Sb_{1.5}Te_3$ (ICDD: 00-049-1713) with rhombohedral crystal structure, and the corresponding indexing of peaks with relevant Miller indices is designated on the diffraction patterns in **Figures 1A–D**. The samples showed a high phase purity. Only in the case of the MA-Bi_2Te_3 sample a diffraction peak at 32° was observed, which is attributed to Te. This peak was not observed in the case of as-milled powder, and its appearance in the SPS processed sample could be due to its evaporation and recrystallization at the pellet surface during the sintering process. The width of the diffraction peaks with the same index is wider for as-made MA samples, which can be ascribed to nonuniform strain within the materials that is generally observed in mechanochemical alloyed samples. During MA, grains in the particle aggregate plastically deformed, possessing a state of uniform tension or compression. The residual strain remaining in the powder after mechanical milling leads to a parallel shift, while the nonuniform strain will lead to broadening of the diffraction peaks (Schaffer and McCormick, 1992). Strain and the crystallite size were calculated for all samples using the Williamson–Hall approach (Mote et al., 2012; Khachotourian et al., 2016; Lim and Quah, 2020), details of which and the results obtained are summarized in **Supplementary Table S1**. MA samples generally show a higher strain for the same sample composition synthesized through the MW route. Upon SPS sintering, the diffraction peaks display a lower peak width, revealing a higher level of ordering and reduced strain for both the MA and MW samples due to the highly energetic consolidation process.

Bi-Sb-Te compounds have a layered crystal structure with anisotropic transport properties. The degree of orientation of these layers/planes determines the texture fraction that plays a major role on the electronic and thermal transport properties. Texture fraction can be interpreted from the peak intensity level of (0 0 *L*) planes, as reported earlier (Hu et al., 2015a; Hu et al., 2018b; Bao et al., 2020), with a higher intensity indicating a higher level of texturing within the structure. It is clear that the SPS process improves texturing in all the materials studied. As can be seen from the XRPD patterns, SPS sintered MW-Bi_2Te_3 (**Figure 1B**) and MW-$Bi_{0.5}Sb_{1.5}Te_3$ (**Figure 1D**) samples display higher (0 0 *l*) peak intensities (or relative peak intensities with respect to the normalized highest intensity diffraction peak) than the MA samples (see **Supplementary Table S2** for intensity of peaks with various Miller indices). This indicates that the MW samples have a higher level of texturing than the MA samples.

The electrical energy consumption of MA and MW reactions can be compared for the typical batches prepared in this work. Using the reaction durations, the electrical energy consumption per gram of MA-Bi_2Te_3 is estimated as 687 kJ/g (4 h milling) and for MA-$Bi_{0.5}Sb_{1.5}Te_3$ (12 h milling) as 2,160 kJ/g, while it is 58 kJ/g for both the MW samples (MW exposure for 6 min). This comparison shows a significant benefit of MW-assisted heating (12 to 40 times lower energy consumption based on the targeted material composition) as a time- and energy-efficient synthetic methodology. Both the methods are scalable; MA can be done in larger jars by maintaining the same sample volume to ball volume and free volume ratio. This may, however, lead to prolonged reaction time to obtain the same phase purity of the material. MW synthesis is more flexible in this respect; the amount of sample per reactor can be increased, while the number of reactors can also be increased in parallel per synthesis run, still maintaining a significantly shorter reaction duration.

Microstructure Analysis

SEM micrographs of as-made and sintered MA- and MW-Bi_2Te_3 samples are presented in **Figure 2**. The as-milled MA sample (**Figure 2A**) shows strongly agglomerated/fused nanoparticles, forming globular structures ranging from sub-100 nm up to few micrometers. The as-made sample through MW (**Figure 2D**) shows primary particles with hexagonal, or truncated-edge hexagonal, platelet morphology, inherited from their rhombohedral layered crystal structure. During the bottom-up MW synthesis route, the particles formed can display morphologies representing their crystal structure, which is known as crystal habit. Various platelets sharing a common axis were also observed. The cross section of hexagonal platelets varies in the range of 100–300 nm, where the thickness is typically around 50 nm. Crystallite size estimated from the XRPD for as-made samples was around 30–40 nm, revealing the polycrystalline character of the observed nanoparticles. Upon sintering, both MA and MW samples formed pellets with a packing density of around 80% (see **Table 1**), where MW-Bi_2Te_3 (**Figures 2E,F**) and MA-Bi_2Te_3 samples (**Figures 2B,C**) display similar grain structures.

The SEM micrographs of as-made and sintered MA- and MW-$Bi_{0.5}Sb_{1.5}Te_3$ samples are presented in **Figure 3**. The as-milled MA sample (**Figure 3A**) shows fused nanoparticles, forming globular structures ranging from 200 nm up to few micrometers in the lateral dimension, similar to MA-Bi_2Te_3. The as-made sample through MW (**Figure 3D**) shows particles with hexagonal platelet morphology, with thickness about 50 nm and lateral size of 100–300 nm. **Figure 3** indicates that there are laterally growing grains in both MA and MW samples after SPS. However, as can be seen clearly, the grain size of the MA sample is much larger than that of the MW samples. This may be interpreted *via* surface energy of nanoparticles. In other words, small particles have higher surface energy and, thus, show more resistance to combining with other particles to form larger grains under high temperature and pressure, than larger grains (Ch'ng and Pan, 2007). Upon sintering, MW-$Bi_{0.5}Sb_{1.5}Te_3$ (**Figure 3E,F**) samples display a much more smaller grain structure than the MA sample (**Figure 3B,C**).

Texturing within the SPS processed materials can be implied from the SEM micrographs of the MA and MW samples (**Figures**

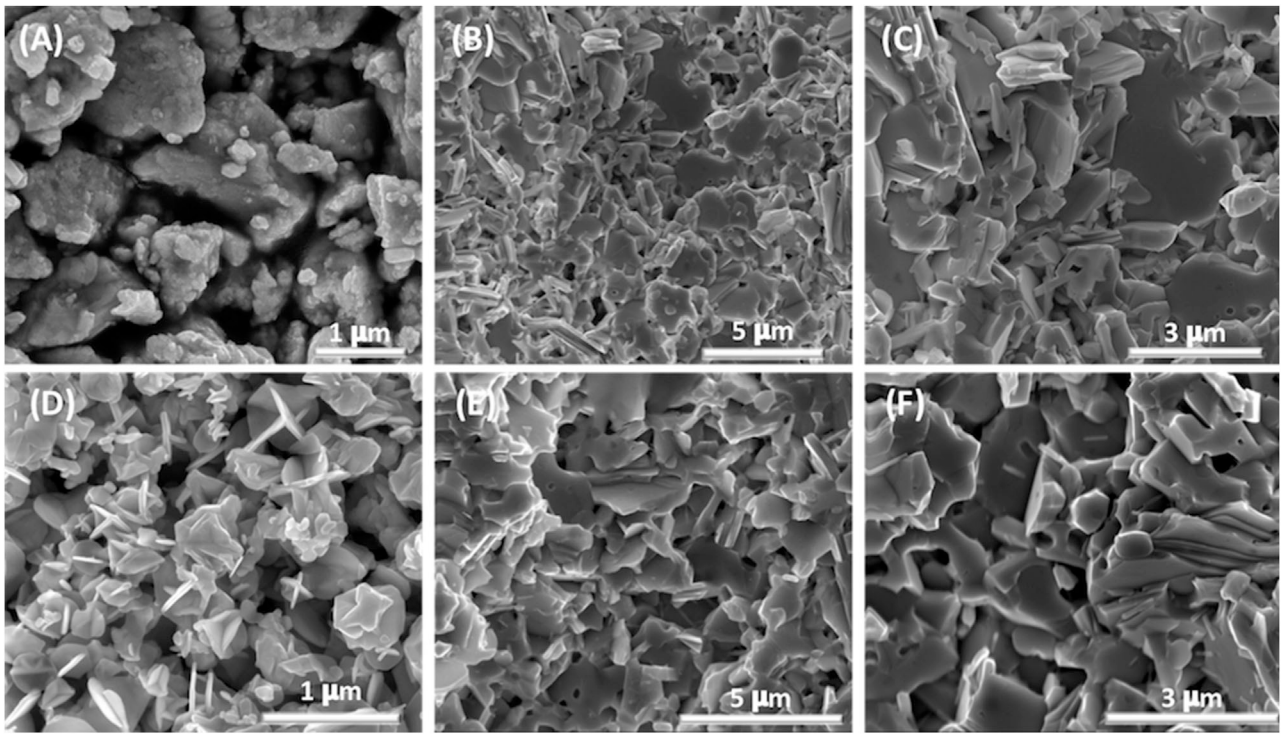

FIGURE 2 | FE-scanning electron microscopy micrographs of **(A)** as-milled MA-Bi_2Te_3, **(D)** as-synthesized MW-Bi_2Te_3, and SPS sintered fractured **(B,C)** MA-Bi_2Te_3 and **(E,F)** MW-Bi_2Te_3.

2, 3). Having the same composition with a different level of texture might be due to different effects of SPS on grains during the compaction. Especially in the case of MW samples, the initial particle morphology being hexagonal may have led to a higher degree of texturing.

Transport Property Evaluation

The transport data in the temperature range from 300 to 523 K are presented in **Figure 4** for sintered MA-Bi_2Te_3 and MW-Bi_2Te_3 samples and in **Figure 5** for MA-$Bi_{0.5}Sb_{1.5}Te_3$ and MW-$Bi_{0.5}Sb_{1.5}Te_3$ samples. **Table 2** also summarizes the transport data at room temperature and at the temperature where the maximum ZT is obtained for the materials with given composition and processing routes.

The electrical conductivity (σ) of MA-Bi_2Te_3 and MW-Bi_2Te_3 samples are shown in **Figure 4A**. They both decrease with increasing temperature, which is a signature of typical highly doped semiconducting behavior. The room temperature σ of MA-Bi_2Te_3 shows higher values (1,250 S/cm) than that of MW-Bi_2Te_3 (1,080 S/cm). The σ of a material is strongly dependent on its carrier density, carrier mobility, energy gap, scattering mechanism of charge carriers, and grain size (Goldsmid, 2010). Due to the absence of Hall measurement data, we cannot comment on the carrier density directly; however, we can infer some points from the bandgap energy. According to Goldsmid's approximation, the energy gap of a TE material can be calculated via maximum value of the Seebeck coefficient and temperature as follows: $2q{\cdot}S_{max}T_{max}$, where q, S_{max}, and T_{max} are electron charge, maximum Seebeck coefficient, and the temperature where the S_{max} was obtained (Goldsmid and Sharp, 1999), respectively. According to this formula, the estimated bandgap for the MA-Bi_2Te_3 sample is approximately 0.16 eV; it is 0.18 eV for the MW-Bi_2Te_3 sample, revealing a smaller energy gap of the MA sample; and for the bulk Bi_2Te_3 sample, it is reported as 0.15 eV (Dannangoda et al., 2018). The estimated bandgap for the samples is larger than that of the bulk material, as an expected outcome of observed nanostructuring from XRPD and SEM (Shevelkov, 2008). Lower bandgap of the MA-Bi_2Te_3 sample is the main reason for its higher σ. Another possible reason is texture within the material and the grain size effect. Since the MA-Bi_2Te_3 sample has larger grains than MW-Bi_2Te_3 samples (see **Figure 2**), its carrier mobility and, thus, σ are higher, which may be linked to its higher electron mean free path. As also noticed in **Figure 4A**, the σ of the MA sample decreases more dramatically with an increase in temperature than that of the MW sample. This may also be ascribed to the smaller energy gap of this sample. The contribution of thermally activated minority carrier is much higher in the sample with a smaller energy gap; therefore, electron–electron, electron–acoustic phonon, and electron–grain boundary scattering increase with increasing temperature, leading to decrease of σ with increasing temperature. The S of MA- and MW-Bi_2Te_3 samples is presented in **Figure 4B**, which clearly indicates electrons as the main charge carriers in both the samples. There is generally an inverse correlation between the electronic conduction and S, which is also observed here for both the samples. The S of MW-Bi_2Te_3

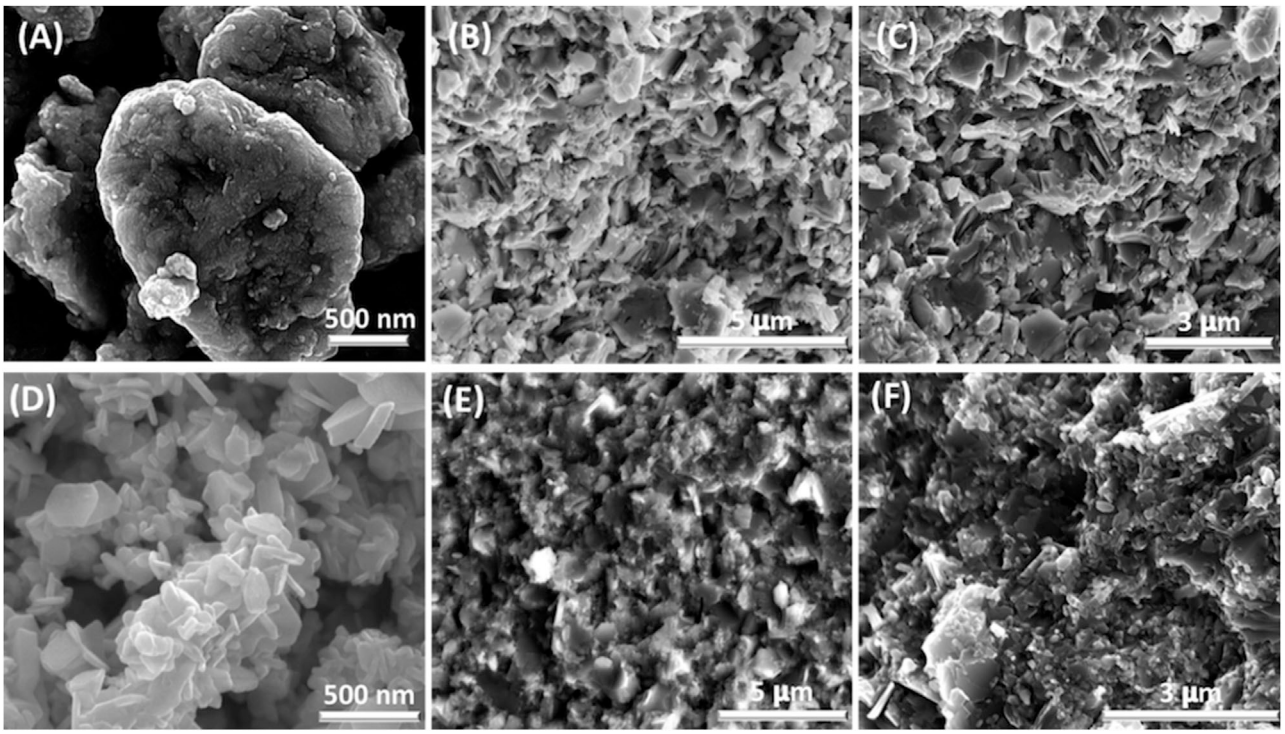

FIGURE 3 | FE-scanning electron microscopy micrographs of **(A)** as-milled MA-$Bi_{0.5}Sb_{1.5}Te_3$, **(D)** as-made MW-$Bi_{0.5}Sb_{1.5}Te_3$, and SPS sintered fractured **(B,C)** MA-$Bi_{0.5}Sb_{1.5}Te_3$ and **(E,F)** MW-$Bi_{0.5}Sb_{1.5}Te_3$.

sample reaches larger absolute values in the whole measurement regime than that of MA-Bi_2Te_3. Scattering mechanism, carrier density, density of states near the Fermi level, and band structure play important roles in the enhancement of *S* (Graziosi et al., 2019).

Electronic transport properties show strong correlation in classical materials; furthermore, they are also strongly affected by charge carrier density, defects, and scattering events, as well as energy bandgap. Therefore, it is possible to observe slightly different transport properties in the materials with the same composition due to its microstructure, which in turn is mostly influenced by the adapted synthetic and processing routes. The MW-Bi_2Te_3 displayed larger energy gap and a blend of micro/nano-size grains, or layers, causing strong scattering of charge carriers and heat carrier phonons (decreased electronic and thermal conductivity), which in turn enhanced the *S* over MA-Bi_2Te_3. The resultant power factor (PF = $S^2\sigma$) is estimated for the Bi_2Te_3 samples, displayed in **Figure 4C**, where the MW-Bi_2Te_3 sample showed a significantly higher PF values than MA-Bi_2Te_3, mostly due to its superior *S* values (max ~21 $\mu WK^2/cm$ at 300 K). This microstructure may serve as an example for energy filtering, where nanostructuring results in higher thermopower ($S^2\sigma$) and lower thermal conductivity, without notably influencing the electrical conductivity as suggested earlier (Shevelkov, 2008).

The σ of MA-$Bi_{0.5}Sb_{1.5}Te_3$ and MW-$Bi_{0.5}Sb_{1.5}Te_3$ samples are presented in **Figure 5A**. MA-$Bi_{0.5}Sb_{1.5}Te_3$ shows almost a flat trend with the σ values in the range of 150–200 S/cm. The MW-$Bi_{0.5}Sb_{1.5}Te_3$ sample shows a decreasing trend of σ with increasing temperature, starting from 400 S/cm at room temperature and reaching 250 S/cm at 523 K. The observed trend for the MW-$Bi_{0.5}Sb_{1.5}Te_3$ sample is similar to heavily doped semiconductors, while that of MA-$Bi_{0.5}Sb_{1.5}Te_3$ is representative of intrinsic semiconductors. The actual composition of the material, energy gap, and carrier density are the three main factors that affect the extrinsic or intrinsic behavior of a material that are determined by the microstructure, defects, and dislocations in the material. Using Goldsmid's approximation (Goldsmid and Sharp, 1999), a lower bandgap is estimated for the MW-$Bi_{0.5}Sb_{1.5}Te_3$ sample than the MA-$Bi_{0.5}Sb_{1.5}Te_3$ sample in agreement with the trend of σ values observed.

The *S* of MA- and MW-$Bi_{0.5}Sb_{1.5}Te_3$ samples is presented in **Figure 5B**, which clearly indicates the p-type (positive *S*) character for both the samples. The trend in magnitude of *S* is inverse of that of σ, as expected. MA-$Bi_{0.5}Sb_{1.5}Te_3$ shows a very high *S* value at room temperature which reduces to about its one-third at 523 K, while MW-$Bi_{0.5}Sb_{1.5}Te_3$ shows an increasing *S* with increasing temperature. The σ slightly increases and the *S* decreases with increasing temperature for the MA-$Bi_{0.5}Sb_{1.5}Te_3$ sample, which can be ascribed to the quite large energy gap of this sample where no strong effect of minority carriers on the transport properties is observed. However, the MW-$Bi_{0.5}Sb_{1.5}Te_3$ sample shows the opposite trend, where the *S* increases and the σ decreases with increasing temperature. This sample might have a smaller energy gap. Thermally activated minority carriers (electrons) are effective on transport properties and reduce the *S* [$(S_h\sigma_h +$

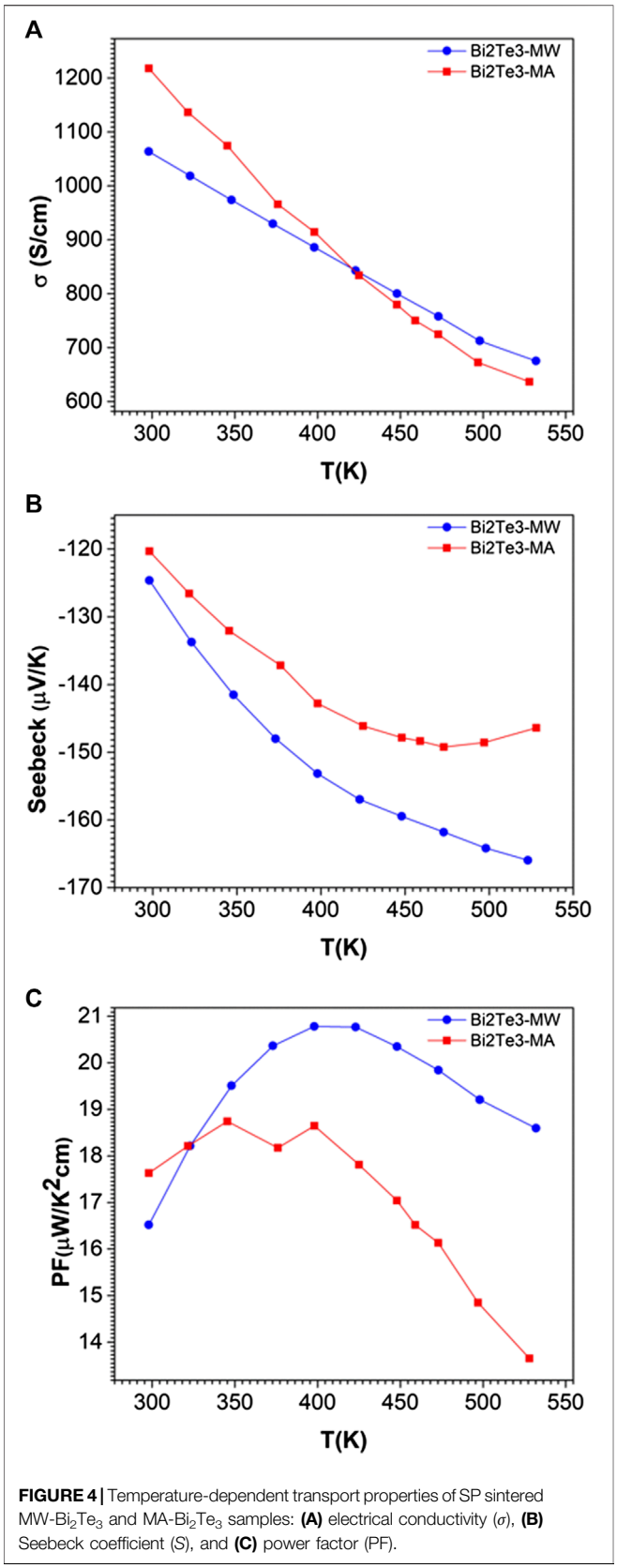

FIGURE 4 | Temperature-dependent transport properties of SP sintered MW-Bi_2Te_3 and MA-Bi_2Te_3 samples: **(A)** electrical conductivity (σ), **(B)** Seebeck coefficient (S), and **(C)** power factor (PF).

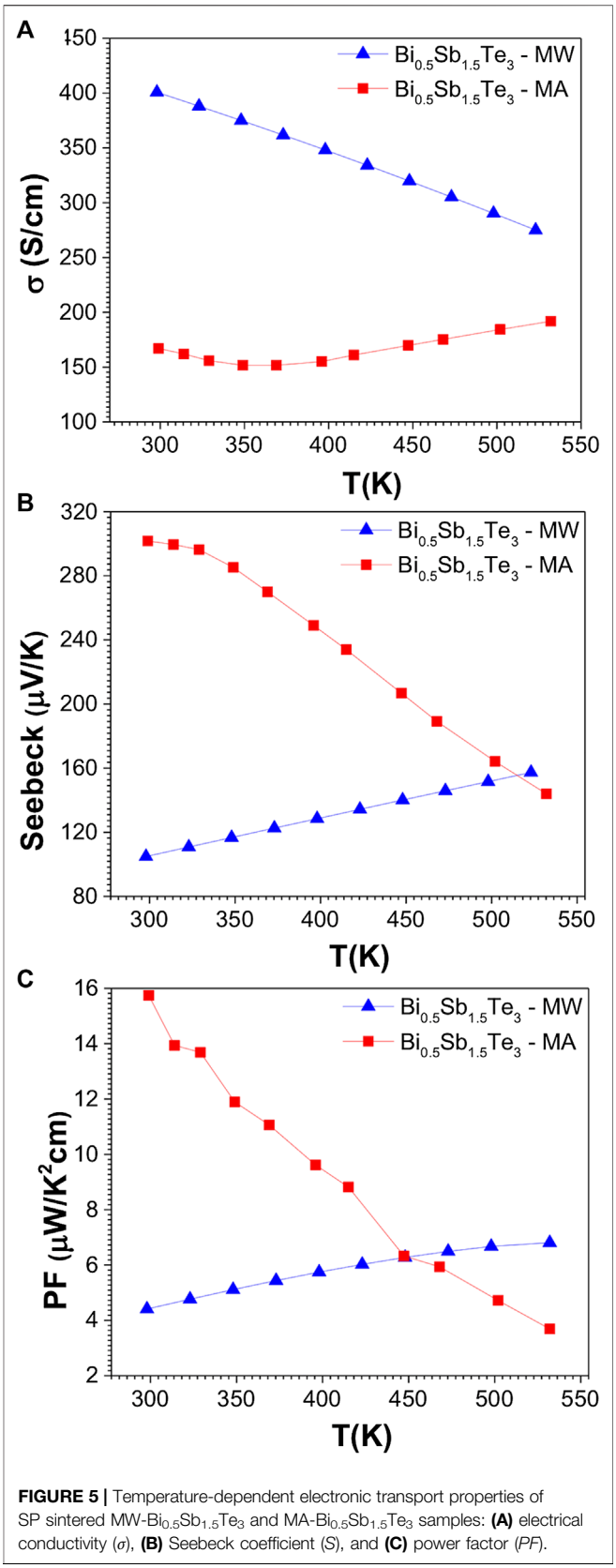

FIGURE 5 | Temperature-dependent electronic transport properties of SP sintered MW-$Bi_{0.5}Sb_{1.5}Te_3$ and MA-$Bi_{0.5}Sb_{1.5}Te_3$ samples: **(A)** electrical conductivity (σ), **(B)** Seebeck coefficient (S), and **(C)** power factor (PF).

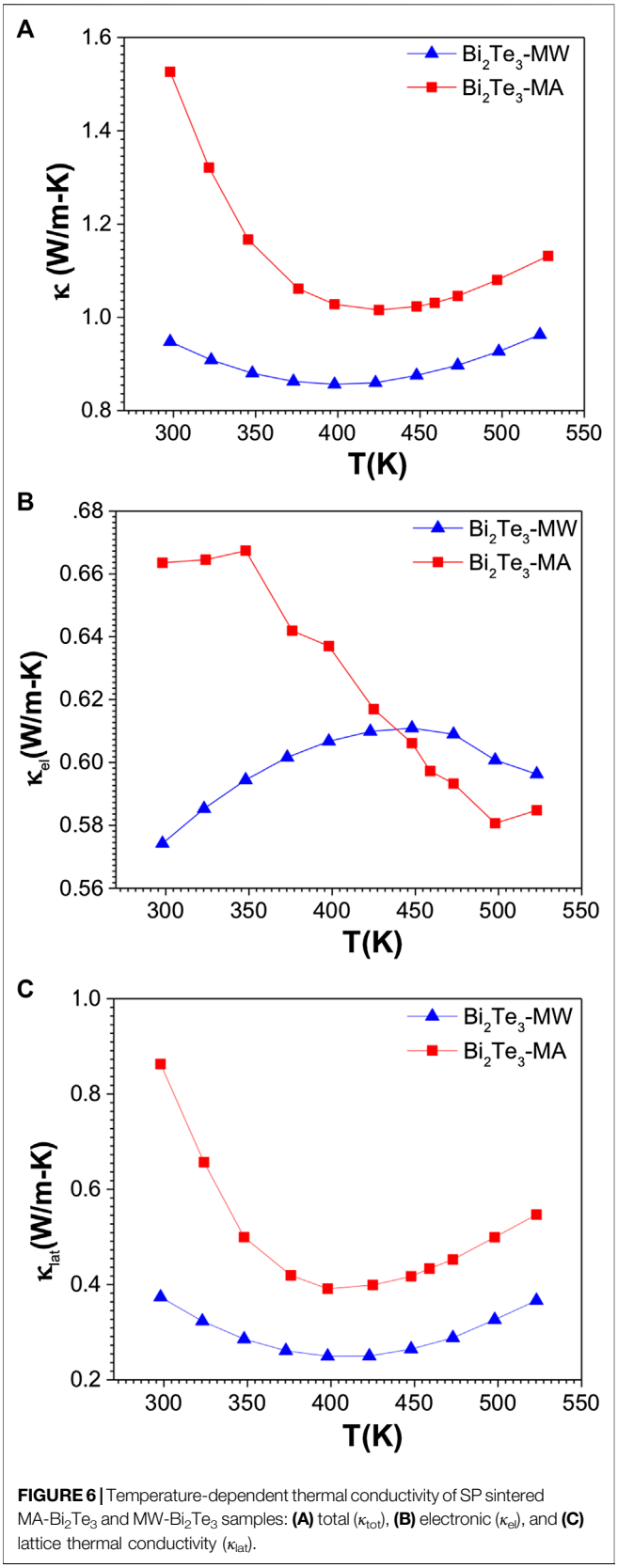

FIGURE 6 | Temperature-dependent thermal conductivity of SP sintered MA-Bi_2Te_3 and MW-Bi_2Te_3 samples: **(A)** total (κ_{tot}), **(B)** electronic (κ_{el}), and **(C)** lattice thermal conductivity (κ_{lat}).

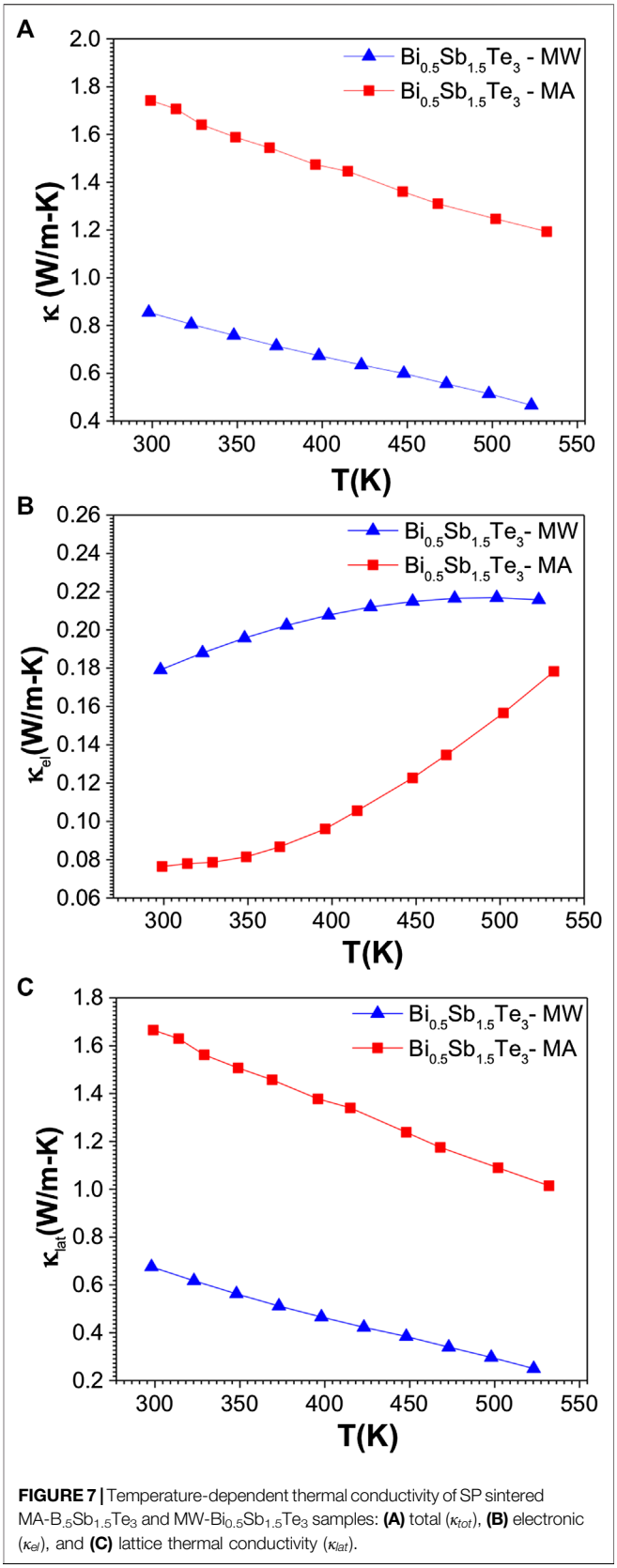

FIGURE 7 | Temperature-dependent thermal conductivity of SP sintered MA-$B_{.5}Sb_{1.5}Te_3$ and MW-$Bi_{0.5}Sb_{1.5}Te_3$ samples: **(A)** total (κ_{tot}), **(B)** electronic (κ_{el}), and **(C)** lattice thermal conductivity (κ_{lat}).

$S_e\sigma_e)/(\sigma_h + \sigma_e)$]. The relationship of the partial S contributions to S_{total} (S_h and S_e) shows that the magnitude of the S is strongly related to the number of charge carriers and their effective mass. Samples with a high concentration of minority carriers show a lower S_{total} (Ballikaya et al., 2013).

The resultant power factor (PF = $S^2\sigma$) is estimated for the $Bi_{0.5}Sb_{1.5}Te_3$ samples, displayed in **Figure 5C**, where MA-$Bi_{0.5}Sb_{1.5}Te_3$ shows significantly higher PF values than the MW sample until the crossover point with MW-$Bi_{0.5}Sb_{1.5}Te_3$ at 450 K. This is certainly ascribed to the very high S observed for MA-$Bi_{0.5}Sb_{1.5}Te_3$.

Thermal conductivity (κ_{tot}) values are calculated for MW-Bi_2Te_3 and MA-Bi_2Te_3 samples from the thermal diffusivity, density of mass, and C_p values, and the results are presented in **Figure 6** as a function of temperature. There is a significant difference between the estimated κ_{tot} values, where MW-Bi_2Te_3 shows values below 1 W/m K in the whole temperature region, while MA-Bi_2Te_3 shows rather high values in the order of 1.55 W/m K at room temperature, which parabolically changes and reaches 1.15 (**Figure 6A**). The parabolic behavior of κ_{tot} of MA-Bi_2Te_3 is attributed to bipolar effects, where it makes a dip around 400 K, reaching 1 W/m K, and increases up to 1.15 with increasing temperature, which supports our argument on thermally activated minority carrier effect. It is well known that grain boundaries behave like scattering centers for phonons, lattice vibrations, which can cause damping of the thermal conductivity. The κ_{tot} of the MW sample is lower than that of bulk ingot Bi_2Te_3 (1.5 W/m K), while that of the MA sample is comparable. Looking at the microstructure of the sintered samples (**Figure 2**), one can easily see the finer grains, and thus a higher grain boundary density in MW-Bi_2Te_3, leading to a lower κ_{tot}.

The calculated κ_{tot} values for MW-$Bi_{0.5}Sb_{1.5}Te_3$ and MA-$Bi_{0.5}Sb_{1.5}Te_3$ samples are presented in **Figure 7**. Both samples show a decreasing trend with increasing temperature. MA-$Bi_{0.5}Sb_{1.5}Te_3$ shows much higher κ_{tot} (**Figure 7A**) values in the order of 1.8 W/m K at room temperature, which monotonically reduces to 1.2 at 523 K. The MW-$Bi_{0.5}Sb_{1.5}Te_3$ sample shows a parallel trend to MA-$Bi_{0.5}Sb_{1.5}Te_3$ with at least about 50% lower κ_{tot} values in the whole temperature range. This significantly lower κ_{tot} values for MW-$Bi_{0.5}Sb_{1.5}Te_3$ is attributed to the finer grain structure, resulting in a higher grain boundary density, effectively scattering phonons.

κ_{tot} has two major contributors: namely, electronic (κ_{el}) and lattice components (κ_{lat}). Nanostructuring have been shown to reduce the thermal conductivity of the material by increased density of grain boundaries, leading to significant phonon scattering, which has a strong influence on κ_{lat} mainly. The Wiedemann–Franz law ($\kappa_{el} = \sigma L_o T$, where σ is the electrical conductivity and L_o is the Lorenz number at a given temperature T) can be used to estimate the electronic contribution (κ_{el}) to κ_{tot}, and thereafter, κ_{lat} can be obtained by simply subtracting κ_{el} from κ_{tot}. The Lorenz number (L_o) as a function of temperature was calculated for all samples, by using the methodology detailed in the **Supplementary Material**. The calculated L_o values (estimated in the range 1.50–1.90 10^{-8} $W\Omega K^{-2}$ at room temperature to 1.70–1.75 10^{-8} $W\Omega/K^2$ at 523 K) were used to estimate κ_{el} and κ_{lat} for all samples; results are displayed in **Figures 6B,C** and **7B,C** for all Bi_2Te_3 and $Bi_{0.5}Sb_{1.5}Te_3$ samples, respectively. In the MA- and MW-Bi_2Te_3 samples, κ_{tot} is dominated by electronic contribution (κ_{el}), while in the MA- and MW-$Bi_{0.5}Sb_{1.5}Te_3$ samples, κ_{lat} predominates the thermal conductivity. This can be ascribed to various scattering events, including phonon-point defect scattering and phonon grain boundary scattering (due to nano-sized grains). It is important to see the significant effect of κ_{lat} on the transport properties, and thus the major role of its reduction in enhancing the ZT value of especially MW-synthesized compositions.

Based on all electronic and thermal transport data, the TE figure of merit, ZT, has been estimated for all samples; the results are presented in **Figure 8** as a function of temperature. MW-Bi_2Te_3 shows ZT of around 0.5 at RT, reaching 1.04 around 440 K. At this point, the trend bends downward, which can be attributed to the increase in the κ_{tot} due to bipolar effect. The MA-Bi_2Te_3 sample shows a similar trend but with about 30–40% lower values, reaching the highest ZT of 0.7 at 440 K $Bi_{0.5}Sb_{1.5}Te_3$ samples exhibit a very different behavior, where the MA-$Bi_{0.5}Sb_{1.5}Te_3$ sample shows a declining ZT by increasing temperature, starting at about 0.3 and reaching down to 0.15 at 523 K. However, the MW-$Bi_{0.5}Sb_{1.5}Te_3$ sample shows a significant increase in the ZT, from 0.15 at room temperature to 0.76 at 523 K. The microstructure of MW samples (smaller grain structure and high density of grain boundaries) allows for decoupling of the thermal transport from the electronic transport by the higher density of grain boundaries/interfaces, leading to increased scattering of phonons (κ_{lat}). The combined overall effects on the electronic and thermal transport properties of the MW samples lead to significantly higher ZT values, revealing the importance of the resultant microstructure in connection to the respective synthesis routes.

CONCLUSIONS

$Bi_{2-x}Sb_xTe_3$ (where x: 0 and 1.5) materials have been prepared using MA and MW heating routes. MW fabricated materials exhibit hexagonal (or truncated hexagonal) platelet particle morphology in agreement with the rhombohedral crystal structure. Energy consumption was estimated from the synthetic protocols where the MW synthesis consumed 12 to 40 times lower energy (per g) than the MA synthesis route. The TE performance of $Bi_{2-x}Sb_xTe_3$ pellets was studied by evaluating electrical conductivity, Seebeck coefficient, and thermal conductivity of the SP sintered materials. Power factor and the TE figure of merit, ZT, thus have been estimated. An important trend is that while MW-synthesized samples showed similar electrical conductivity values to MA samples, they consistently demonstrated much lower thermal conductivity values, resulting in higher ZT. The highest ZT values were obtained for MW samples, specifically as 1.04 (at 440 K) for MW-Bi_2Te_3 and 0.76 (at 523 K) for MW-$Bi_{0.5}Sb_{1.5}Te_3$. The large density of grain boundaries has been effective in reducing the thermal

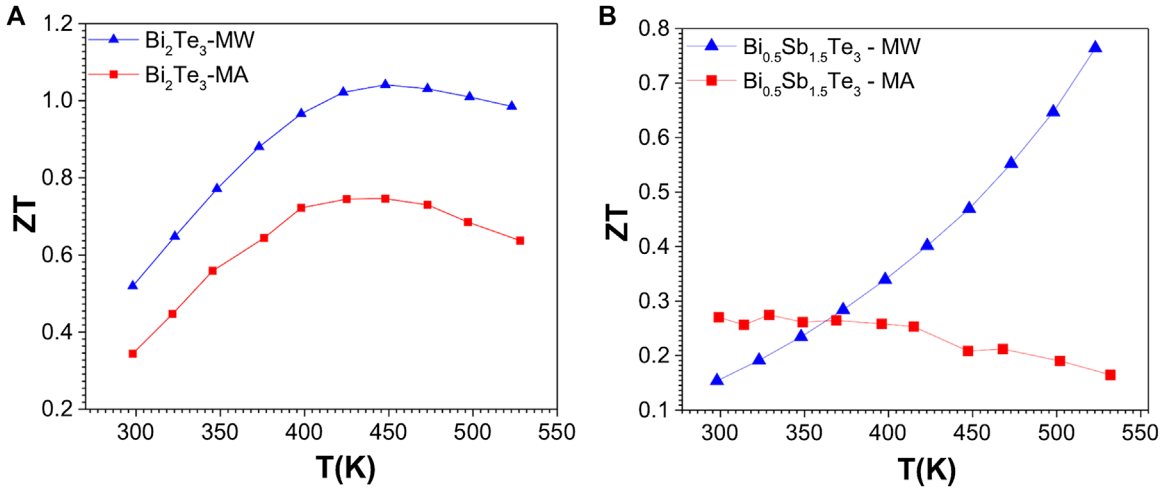

FIGURE 8 | Temperature-dependent TE figure of merit, *ZT*, of **(A)** MW-Bi_2Te_3 and MA-Bi_2Te_3, and **(B)** MW-$Bi_{0.5}Sb_{1.5}Te_3$ and MA-$Bi_{0.5}Sb_{1.5}Te_3$ samples.

conductivity of MW-synthesized materials, thus making it possible to achieve higher ZT values than those synthesized through the MA route. These results, along with the time and energy efficiency, confirm the MW-assisted solution synthesis route as an alternative viable and scalable route for promising nanostructured TE material synthesis, besides powder metallurgical routes.

DATA AVAILABILITY STATEMENT

The original contributions presented in the study are included in the article/**Supplementary Material**. Further inquiries can be directed to the corresponding author.

AUTHOR CONTRIBUTIONS

MST conceived of the presented idea. BH and HM contributed to conceptualization and methodology, material synthesis, and original draft preparation. All authors discussed the results, and reviewed and edited the manuscript. BH, MO, and NB contributed to physicochemical characterization. SB and YD validated the TE properties. MST, SB, and SAS supervised the work. All authors have read and agreed to the published version of the manuscript.

FUNDING

This work was supported by the Swedish Energy Agency (Energimyndigheten, 43521–1) and in part by the Swedish Research Council (VR, 2018–03462). SB acknowledges support by the Scientific and Technological Research Council of Turkey (TUBITAK, 119N120) and Scientific Research Projects Coordination Unit of Istanbul University (BAP 35577 and 32641). SAS acknowledges support by the Deputy of Research and Technology of Ferdowsi University of Mashhad. MST acknowledges financial support from the Olle Engkvist Foundation (SOEB) (190–0315) for the establishment of microwave synthesis facilities.

SUPPLEMENTARY MATERIAL

The Supplementary Material for this article can be found online at: https://www.frontiersin.org/articles/10.3389/fmats.2020.569723/full#supplementary-material

REFERENCES

Aktaş, S., and Diler, E. A. (2018). A review on the effects of micro-nano particle size and volume fraction on microstructure and mechanical properties of metal matrix composites manufactured via mechanical alloying. *Int. Adv. Res. Eng. J.* 2 (1), 68–74.

Anastas, P. T., and Lankey, R. L. (2002). Sustainability through green chemistry and engineering. *ACS Symp. Ser.* 819 (3):1–9. doi:10.1021/bk-2002-0819.ch001

Ballikaya, S., Uzar, N., Yildirim, S., and Salvador, J. R. (2013). Electrical and thermal properties of Fe substituted double-filled $Ba_xYb_yFe_zCo_{4-z}Sb_{12}$ skutterudites. *J. Solid State Chem.* 197, 440–446. doi:10.1016/j.jssc.2012.08.025

Bao, D., Chen, J., Yu, Y., Liu, W., Huang, L., Han, G., et al. (2020). Texture-dependent thermoelectric properties of nano-structured Bi2Te3. *Chem. Eng. J.* 388, 124295. doi:10.1016/j.cej.2020.124295

Boyer, A., and Cissé, E. (1992). Properties of thin film thermoelectric materials: application to sensors using the Seebeck effect. *Mater. Sci. Eng. B.* 13 (2), 103–111. doi:10.1016/0921-5107(92)90149-4

Cao, Y. Q., Zhao, X. B., Zhu, T. J., Zhang, X. B., and Tu, J. P. (2008a). Syntheses and thermoelectric properties of Bi_2Te_3-Sb_2 Te_3 bulk nanocomposites with laminated nanostructure. *Appl. Phys. Lett.* 92 (14), 90–93. doi:10.1063/1.2900960

Cao, Y. Q., Zhu, T. J., Zhao, X. B., Zhang, X. B., and Tu, J. P. (2008b). Nanostructuring and improved performance of ternary Bi-Sb-Te

thermoelectric materials. *Appl. Phys. A* 92 (2), 321–324. doi:10.1007/s00339-008-4518-y

Ch'ng, H. N., and Pan, J. (2007). Sintering of particles of different sizes. *Acta Mater.* 55 (3), 813–824. doi:10.1016/j.actamat.2006.07.015

Dannangoda, G. C., Key, C., Sumets, M., and Martirosyan, K. S. (2018). Transition of p- to n-type conductivity in mechanically activated bismuth telluride. *J. Electron. Mater.* 47 (10), 5800–5809. doi:10.1007/s11664-018-6469-1

Dresselhaus, M. S., Dresselhaus, G., Sun, X., Zhang, Z., Cronin, S. B., and Koga, T. (1999). Low-dimensional thermoelectric materials. *Phys. Solid State*. 41 (5), 679–682. doi:10.1134/1.1130849

Goldsmid, H. (2010). *Introduction to thermoelectricity*. 1st Edn. *Springer series in materials science*. Netherlands: Springer. Vol. 121.

Goldsmid, H. J., and Sharp, J. W. (1999). Estimation of the thermal band gap of a semiconductor from Seebeck measurements. *J. Electron. Mater.* 28 (7), 869–872. doi:10.1007/s11664-999-0211-y

Graziosi, P., Kumarasinghe, C., and Neophytou, N. (2019). Impact of the scattering physics on the power factor of complex thermoelectric materials. *J. Appl. Phys.* 126, 155701. doi:10.1063/1.5116793

Hamawandi, B., Ballikaya, S., Råsander, M., Halim, J., Vinciguerra, L., and Rosen, J. (2020a). Composition tuning of nanostructured binary copper selenides through rapid chemical synthesis and their thermoelectric property evaluation. *Nanomaterials* 10 (5), 854. doi:10.3390/nano10050854

Hamawandi, B., Ballikaya, S., Batili, H., Roosmark, V., Orlovská, M., Yusuf, A., et al. (2020b). Facile solution synthesis, processing and characterization of n-and p-type binary and ternary Bi-Sb tellurides. *Appl. Sci.*10 (3). doi:10.3390/app10031178

Harpeness, R., and Gedanken, A. (2003). Microwave-assisted synthesis of nanosized Bi_2Se_3. *New J. Chem.* 27 (8), 1191–1193. doi:10.1039/b300050h

Hicks, L. D., and Dresselhaus, M. S. (1993a). Effect of quantum-well structures on the thermoelectric figure of merit. *Phys. Rev. B* 47 (19), 12727–12731. doi:10.1103/physrevb.47.12727

Hicks, L. D., and Dresselhaus, M. S. (1993b). Thermoelectric figure of merit of a one-dimensional conductor. *Phys. Rev. B* 47 (24), 16631–16634. doi:10.1103/physrevb.47.16631

Hu, L., Wu, H., Zhu, T., Fu, C., He, J., Ying, P., et al. (2015). Tuning multiscale microstructures to enhance thermoelectric performance of n-type bismuth-telluride-based solid solutions. *Adv. Energy Mater.* 5 (17), 1–13. doi:10.1002/aenm.201500411

Hu, L., Zhang, Y., Wu, H., Liu, Y., Li, J., He, J., et al. (2018). Synergistic compositional–mechanical–thermal effects leading to a record high zT in n-type V2VI3 alloys through progressive hot deformation. *Adv. Funct. Mater.* 28 (35), 1–13. doi:10.1002/adfm.201803617

Jang, K. W., Kim, H. J., Jung, W. J., and Kim, I. H. (2018). Charge transport and thermoelectric properties of P-type $Bi_{2-x}Sb_xTe_3$ prepared by mechanical alloying and hot pressing. *J. Korean Inst. Met. Mater.* 56 (1), 66–71. doi:10.3365/kjmm.2018.56.7.544

Jiang, Y., and Zhu, Y.-J. (2007). Bi_2Te_3 nanostructures prepared by microwave heating. *J. Cryst. Growth* 306 (2), 351–355. doi:10.1016/j.jcrysgro.2007.05.012

Khachatourian, A. M., Golestani-Fard, F., Sarpoolaky, H., Vogt, C., Vasileva, E., Mensi, M., et al. (2016). Microwave synthesis of Y2O3:Eu3+ nanophosphors: a study on the influence of dopant concentration and calcination temperature on structural and photoluminescence properties. *J. Lumin.* 169:1–8. doi:10.1016/j.jlumin.2015.08.059

Kumar, A., Kuang, Y., Liang, Z., and Sun, X. (2020). Microwave chemistry, recent advancements, and eco-friendly microwave-assisted synthesis of nanoarchitectures and their applications: a review. *Mater. Today Nano* 11, 100076. doi:10.1016/j.mtnano.2020.100076

Li, S., Toprak, M. S., Soliman, H. M. A., Zhou, J., Muhammed, M., Platzek, D., et al. (2006). Fabrication of nanostructured thermoelectric bismuth telluride thick films by electrochemical deposition. *Chem. Mater.* 18 (16), 3627–3633. doi:10.1021/cm060171o

Li, S., Liang, Y., Qin, J., Toprak, M., and Muhammed, M. (2009). Template electrodeposition of ordered bismuth telluride nanowire arrays. *J. Nanosci. Nanotechnol.* 9 (2), 1543–1547. doi:10.1166/jnn.2009.c198

Li, S., Zhang, S., He, Z., Toprak, M., Stiewe, C., Muhammed, M., et al. (2010). Novel solution route synthesis of low thermal conductivity nanocrystalline bismuth telluride. *J. Nanosci. Nanotechnol.* 10 (11), 7658–7662. doi:10.1166/jnn.2010.2775

Lim, W. F., and Quah, H. J. (2020). Wet oxidation growth of hafnium doped tantalum oxide films with different composition deposited on silicon substrate. *Appl. Surf. Sci.* 526, 146722. doi:10.1016/j.apsusc.2020.146722

Liu, X. D., and Park, Y. H. (2002). Structure and transport properties of $(Bi_{1-x}Sb_x)_2Te_3$ thermoelectric materials prepared by mechanical alloying and pulse discharge sintering. *Mater. Trans.* 43 (4), 681–687. doi:10.2320/matertrans.43.681

Madavali, B., Kim, H. S., Lee, K. H., Isoda, Y., Gascoin, F., and Hong, S. J. (2016). Large scale production of high efficient and robust p-type Bi-Sb-Te based thermoelectric materials by powder metallurgy. *Mater. Des.* 112, 485–494. doi:10.1016/j.matdes.2016.09.089

Mamur, H., Bhuiyan, M. R. A., Korkmaz, F., and Nil, M. (2018). A review on bismuth telluride (Bi_2Te_3) nanostructure for thermoelectric applications. *Renew. Sustain. Energy Rev.* 82, 4159–4169. doi:10.1016/j.rser.2017.10.112

Mote, V., Purushotham, Y., and Dole, B. (2012). Williamson-Hall analysis in estimation of lattice strain in nanometer-sized ZnO particles. *J. Theor. Appl. Phys.* 6 (1), 2–9. doi:10.1186/2251-7235-6-6

Nüchter, M., Ondruschka, B., Bonrath, W., and Gum, A. (2004). Microwave assisted synthesis–a critical technology overview. *Green Chem.* 6 (3), 128–141. doi:10.1039/b310502d

Pradhan, S., Das, R., Bhar, R., Bandyopadhyay, R., and Pramanik, P. (2017). A simple fast microwave-assisted synthesis of thermoelectric bismuth telluride nanoparticles from homogeneous reaction-mixture. *J. Nanoparticle Res.* 19 (2). doi:10.1007/s11051-017-3745-6

Prasad, S., Kumar, V., Kirubanandam, S., and Barhoum, A. (2018). "Engineered nanomaterials: nanofabrication and surface functionalization," in *Emerging applications of nanoparticles and architectural nanostructures: current prospects and future trends*. Amsterdam, Netherlands: Elsevier, 305–340. doi:10.1016/B978-0-323-51254-1/00011-7

Prieto, A. L., Sander, M. S., Martín-González, M. S., Gronsky, R., Sands, T., and Stacy, A. M. (2001). Electrodeposition of ordered Bi_2Te_3 nanowire arrays. *J. Am. Chem. Soc.* 123 (29), 7160–7161. doi:10.1021/ja015989j

Rowe, D. M. (2018). *Thermoelectrics handbook-macro to nano*. Boca Raton, FL, USA: CRC Press. doi:10.1201/9781420038903

Saleemi, M., Toprak, M. S., Li, S., Johnsson, M., and Muhammed, M. (2012). Synthesis, processing, and thermoelectric properties of bulk nanostructured bismuth telluride (Bi_2Te_3). *J. Mater. Chem.* 22 (2), 725–730. doi:10.1039/c1jm13880d

Schaffer, G. B., and McCormick, P. G. (1992). "Mechanical alloying," in *Metals forum*, Vol. 16, 91–97. doi:10.4028/www.scientific.net/MSF.88-90.779

Shevelkov, A. V. (2008). Chemical aspects of the design of thermoelectric materials. *Russ. Chem. Rev.* 77 (1), 1–19. doi:10.1070/rc2008v077n01abeh003746

Shi, W., Zhou, L., Song, S., Yang, J., and Zhang, H. (2008). Hydrothermal synthesis and thermoelectric transport properties of impurity-free antimony telluride hexagonal nanoplates. *Adv. Mater.* 20 (10), 1892–1897. doi:10.1002/adma.200702003

Snyder, G. J., and Toberer, E. S. (2010). Complex thermoelectric materials. *Mater. Sci. Eng.* 7, 101–110. doi:10.1142/9789814317665_0016

Stojanovic, B. D., Jovalekic, C., Vukotic, V., Simoes, A. Z., and Varela, J. A. (2005). Ferroelectric properties of mechanically synthesized nanosized barium titanate. *Ferroelectrics* 319, 65–73. doi:10.1080/00150190590965424

Xiao, F., Yoo, B., Lee, K. H., and Myung, N. V. (2007). Synthesis of Bi_2Te_3 nanotubes by galvanic displacement. *J. Am. Chem. Soc.* 129 (33), 10068–10069. doi:10.1021/ja073032w

Yao, Q., Zhu, Y., Chen, L., Sun, Z., and Chen, X. (2009). Microwave-assisted synthesis and characterization of Bi_2Te_3 nanosheets and nanotubes. *J. Alloys Compd.* 481 (1–2), 91–95. doi:10.1016/j.jallcom.2009.03.001

Yu, H., Gibbons, P. C., and Buhro, W. E. (2004). Bismuth, tellurium, and bismuth telluride nanowires. *J. Mater. Chem.* 14, 595–602. doi:10.1039/b312820b

Zakeri, M., Ramezani, M., and Nazari, A. (2012). Effect of ball to powder weight ratio on the mechanochemical synthesis of $MoSi_2$-TiC nanocomposite powder. *Mater. Res.* 15 (6), 891–897. doi:10.1590/s1516-14392012005000111

Zhang, C., Peng, Z., Li, Z., Yu, L., Khor, K. A., and Xiong, Q. (2015). Controlled growth of bismuth antimony telluride Bi Sb_2–Te_3 nanoplatelets and their bulk

thermoelectric nanocomposites. *Nanomater. Energy* 15, 688–696. doi:10.1016/j.nanoen.2015.05.022

Zhao, X. B., Ji, X. H., Zhang, Y. H., Zhu, T. J., Tu, J. P., and Zhang, X. B. (2005). Bismuth telluride nanotubes and the effects on the thermoelectric properties of nanotube-containing nanocomposites. *Appl. Phys. Lett.* 86 (6), 1–3. doi:10.1063/1.1863440

Zhou, B., Zhao, Y., Pu, L., and Zhu, J.-J. (2006). Microwave-assisted synthesis of nanocrystalline Bi_2Te_3. *Mater. Chem. Phys.* 96, 192–196. doi:10.1016/j.matchemphys.2005.07.010

Zhou, B., and Zhu, J. J. (2009). Microwave-assisted synthesis of Sb_2Se_3 submicron rods, compared with those of Bi_2Te_3 and Sb_2Te_3. *Nanotechnology* 20 (8). doi:10.1088/0957-4484/20/8/085604

Conflict of Interest: The authors declare that the research was conducted in the absence of any commercial or financial relationships that could be construed as a potential conflict of interest.